

Twisted Pseudodisk and Asymmetric Mass Accretion on the Circumstellar Disk

MASAHIRO N. MACHIDA,^{1,2} SHANTANU BASU,^{3,2} AND SHINGO HIRANO⁴

¹*Department of Earth and Planetary Sciences, Faculty of Science, Kyushu University, Fukuoka 819-0395, Japan*

²*Department of Physics and Astronomy, University of Western Ontario, London, ON N6A 3K7, Canada*

³*Canadian Institute for Theoretical Astrophysics, University of Toronto, 60 St. George St., Toronto, ON M5S 3H8, Canada*

⁴*Department of Applied Physics, Faculty of Engineering, Kanagawa University, Kanagawa 221-0802, Japan*

ABSTRACT

We model gas inflow patterns onto circumstellar disks and the evolution of the pseudodisk using three-dimensional resistive MHD simulations. Starting from a prestellar core without turbulence and with a misalignment between the initial magnetic field and rotation axis, the simulations are performed for $\sim 10^5$ yr after protostar formation. After disk formation, the magnetic field around the disk becomes significantly distorted due to the disk rotational motion. Consequently, the structure of the pseudodisk also evolves into a complex morphology. As a result, both accretion onto the disk and outflow become asymmetric and anisotropic. Accretion to the disk occurs primarily through narrow-channel flows or streams. The time evolution of the infalling envelope leads to non-steady accretion onto the disk, which in turn causes variability in the mass accretion onto the central protostar. This study demonstrates that complex infalling envelope structures and channelized accretion flows onto the disk naturally arise even without assuming turbulence or external asymmetric inflows.

Keywords: Magnetohydrodynamical simulations (1966) — Protostars (1302) — Protoplanetary disks (1300) — Circumstellar disks (235) — Stellar jets (1807) — Star formation (1569)

1. INTRODUCTION

Observations have revealed that molecular cloud cores, which are the birthplaces of stars, are threaded by coherent magnetic fields (e.g., Planck Collaboration et al. 2016). In such cores, the magnetic energy dominates over the rotational energy and is comparable to the gravitational energy (Crutcher et al. 2010; Caselli et al. 2002). As a result, gravitational collapse preferentially occurs along magnetic field lines, which leads to the formation of a flattened, disk-like structure known as a pseudodisk (Galli & Shu 1993). The pseudodisk persists even after the formation of a protostar and surrounds the circumstellar disk as an extended structure (e.g., Basu et al. 2024). Although the pseudodisk forms due to the anisotropic Lorentz force, it is not supported against gravity and therefore continues to collapse. The contraction proceeds more slowly than in the non-magnetized case due to the influence of the magnetic field (Hirano et al. 2025). Accretion onto the disk or protostar occurs through the pseudodisk, which corresponds to the infalling envelope (Machida & Hosokawa 2013).

Recent high-resolution ALMA observations have revealed complex structures around circumstellar disks (Tokuda et al. 2014, 2016; Yen et al. 2019; Pineda et al. 2020). Some of these features can be explained by interchange instability occurring at the outer edge of the disk (Tokuda et al. 2023, 2024; Fielder et al. 2024; Tanius et al. 2024), but more extended and irregular structures have also been detected, which cannot be accounted for by this mechanism alone (for details, see Pineda et al. 2023). Moreover, asymmetric gas accretion onto circumstellar disks has been reported (e.g., Garufi et al. 2022; Valdivia-Mena et al. 2022; Choudhury et al. 2025; Kido et al. 2025). In the conventional

machida.masahiro.018@m.kyushu-u.ac.jp

basu@uwo.ca

hirano0613@gmail.com

picture, accretion onto the disk via the pseudodisk is expected to occur in an axisymmetric fashion (Tomisaka 1995, 1996; Basu & Mouschovias 1994, 1995a,b; Machida et al. 2005, 2006). Consequently, recent observations of asymmetric accretion have often been interpreted as resulting from gas inflow outside the molecular cloud core, the infall of small gas clumps, or internal turbulence within the core (Pineda et al. 2023).

Many previous simulation studies about collapsing star-forming cores have assumed, for simplicity, that the angular momentum vector of the molecular cloud core is aligned with the global magnetic field threading the core (see review by Tsukamoto et al. 2023). However, both observations and simulations suggest that these directions are not necessarily parallel (e.g., Hull et al. 2013; Misugi et al. 2024). We have previously studied the early evolution of molecular cloud cores with misaligned magnetic fields and angular momentum vectors using three-dimensional simulations, focusing on disk formation and the development of outflows and jets shortly after protostar formation (Kataoka et al. 2012; Shinnaga et al. 2012; Hirano & Machida 2019; Hirano et al. 2020; Machida et al. 2020). However, the long-term evolution of the pseudodisk and the pattern of accretion onto the disk have not been explored in detail. In this study, we investigate the long-term evolution of pseudodisks and accretion patterns in collapsing molecular cloud cores, where the global magnetic field is initially misaligned with the angular momentum vector.

2. NUMERICAL SETTINGS AND INITIAL CONDITIONS

Since the numerical settings and initial conditions are almost the same as our previous studies (Kataoka et al. 2012; Hirano & Machida 2019; Machida et al. 2020), we describe them briefly. As the initial condition, we adopt a critical Bonnor–Ebert sphere with a central density $n_{c,0} = 10^4 \text{ cm}^{-3}$ and an isothermal temperature $T = 10 \text{ K}$. To induce gravitational collapse, the density is enhanced by a factor of $f = 1.68$ (Machida & Basu 2024). The mass and radius of the initial cloud are $M_{\text{cl},0} = 8.1 M_{\odot}$ and $R_{\text{cl},0} = 4.8 \times 10^4 \text{ au}$, respectively. The computational boundary is placed at a distance $16 R_{\text{cl},0}$ from the cloud center to suppress reflections of Alfvén waves generated within the cloud ($r < R_{\text{cl},0}$) (Machida & Hosokawa 2013). Gravity is turned off outside the initial cloud ($r > R_{\text{cl},0}$), and inflow from the ambient medium is prohibited (Machida & Hosokawa 2020). In contrast, the mass outflow from the cloud ($r < R_{\text{cl},0}$) to the interstellar region ($r > R_{\text{cl},0}$) is allowed to adequately account for protostellar outflows (Basu et al. 2024).

A uniform magnetic field $B_0 = 5.5 \times 10^{-6} \text{ G}$ is imposed across the entire computational domain. The mass-to-flux ratio of the initial cloud is $\mu_0 = 3$, normalized by the critical value $(2\pi G^{1/2})^{-1}$. Rigid rotation with an angular velocity $\Omega_0 = 2.5 \times 10^{-14} \text{ s}^{-1}$ is imposed within the initial cloud ($r < R_{\text{cl},0}$). The ratios of thermal, rotational, and magnetic energies to the gravitational energy are $\alpha_0 = 0.5$, $\beta_0 = 0.02$, and $\gamma_0 = 0.1$, respectively. Each energy component is numerically calculated within the initial cloud ($r < r_{\text{cl},0}$). In this paper, we present the results for the model with an angle $\theta_0 = 30^\circ$ between the initial magnetic field direction and angular momentum vector.

To follow the cloud evolution, we use our nested-grid code (Machida et al. 2004, 2005, 2010, 2014; Machida 2021). Each cubic grid consists of $(i, j, k) = (64, 64, 64)$ cells. Initially, five grid levels ($l = 1\text{--}5$) are nested, where the level of refinement is denoted by the index l . The initial cloud is embedded in the fifth grid level ($l = 5$), which has a box size of $L(5) = 9.5 \times 10^4 \text{ au}$ and a cell width of $h(5) = 1.5 \times 10^3 \text{ au}$. The maximum grid level is set to $l = 16$. The coarsest grid ($l = 1$) has a box size of $L(1) = 1.5 \times 10^6 \text{ au}$ and a cell width of $h(1) = 2.3 \times 10^4 \text{ au}$. The finest grid ($l = 16$) has a box size of $L(16) = 46 \text{ au}$ and a cell width of $h(16) = 0.73 \text{ au}$. As the cloud begins to collapse, finer grids are automatically generated to ensure that the local Jeans wavelength is resolved by at least 16 cells.

When the density exceeds $n_{\text{sink}} = 10^{13} \text{ cm}^{-3}$ in the collapsing cloud, a sink cell is introduced at the center of the computational domain, and its position is kept fixed throughout the calculation (Machida et al. 2010). After the sink is created, 1% of the gas exceeding n_{sink} within the sink radius of $r_{\text{sink}} = 1 \text{ au}$ is removed from the computational domain and added to the protostellar mass (Machida et al. 2014, 2016). The magnetic flux associated with the gas accreted onto the sink is not removed from the computational domain in order to maintain the divergence-free condition of the magnetic field. Because the initial conditions maintain point symmetry about the center of the computational domain, fixing the sink at the origin is justified in this study. However, small center-of-mass drifts may still arise from numerical round-off, and therefore this approach is not universally applicable (Hirano et al. 2020).

3. RESULTS

We performed simulations of molecular cloud core evolution for approximately 100,000 years after protostar formation. During this period, the protostar increased its mass to $0.45 M_{\odot}$. Figure 1 shows the density distribution at the end of the simulation. The top and middle panels display cross sections on the $y = 0$, $x = 0$, and $z = 0$ planes, centered on the protostar and disk region, at spatial scales of $\sim 1,000 \text{ au}$ (top) and $\sim 10,000 \text{ au}$ (middle). The bottom panels

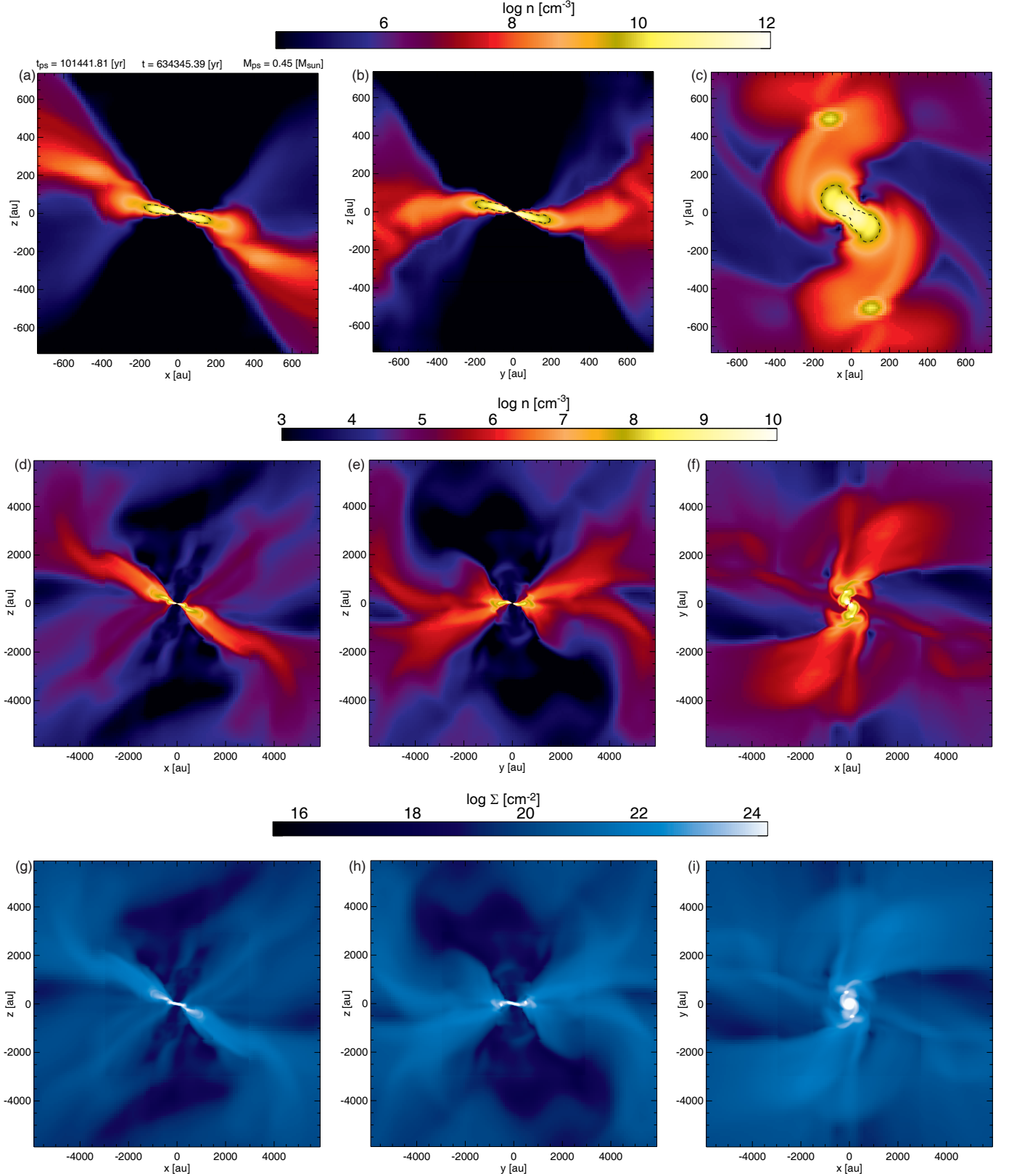


Figure 1. (a)–(f): Density (color) distribution on the $x = 0$ (panels (a) and (d)), $y = 0$ (panels (b) and (e)), and $z = 0$ (panels (c) and (f)) planes. (g)–(i): Surface density (color) distributions on the $x = 0$ (panel (g)), $y = 0$ (panel (h)), and $z = 0$ (panel (i)) planes. The dotted curves in panels (a)–(c) indicate the rotationally supported disk. The elapsed time t_{ps} after protostellar formation, the time t since the onset of cloud collapse, and the protostellar mass are indicated in panel (a). The spatial scale in panels (a)–(c) differs from that in panels (d)–(f) and (g)–(i). An animated version of this figure is available. In the animation, the time sequence of the density and velocity distribution on the $x = 0$, $y = 0$, and $z = 0$ plane as in Figure 1 from the beginning until the end of the simulation is shown. The duration of the animation is 25 s.

show the corresponding surface density distributions. A rotationally supported disk is indicated by the dotted curves in panels (a)–(c)¹.

As seen in Figures 1(a) and 1(c), the rotationally supported disk has a size of ~ 300 au, while the surrounding disk-like structure extends well beyond it. Figure 1(a) and 1(b) show that the outer disk-like structure is misaligned with respect to the inner disk. The inner structure corresponds to the rotationally supported disk, while the outer structure corresponds to the pseudodisk. Since the rotation axis of the circumstellar disk and the normal vector of the pseudodisk are not aligned, the pseudodisk becomes twisted and deformed as the disk grows around the protostar (for detailed explanation see Hirano & Machida 2019). The clumps located above and below the center in Figure 1(c) are not gravitationally bound, and they represent transient high-density structures formed as a result of the twisting of the pseudodisk (Machida et al. 2020).

Figures 1(d) and 1(e) show that the pseudodisk (or infalling envelope) extends diagonally from the upper left to the lower right (panel d), or from the lower left to the upper right (panel e), with respect to the protostar. The structures seen in the cross-sectional views are also visible in the surface density maps, indicating that the infalling envelope is neither axisymmetric nor spherically symmetric. The vertical cavities above and below the disk in Figures 1(d), 1(e), 1(g) 1(h) are carved out by the outflow. It should be noted that, because only an initial misalignment between the rotation axis and the magnetic field was introduced, the overall structure remains approximately point-symmetric with respect to the protostar.

Figure 2 shows the three-dimensional structures of the pseudodisk (infalling envelope) and the rotationally supported disk at different spatial scales. Each panel presents an iso-density surface at a specified number density n_{surf} . Figure 2(a) shows that a smooth disk structure exists within approximately 300 au from the center, corresponding to the rotationally supported disk. At a larger scale of 3,000 au, shown in Figure 2(b), the structure exhibits an overall disk-like morphology but is geometrically distorted. This structure is not supported by rotation and continues to collapse, with gas accreting onto the central region through narrow channels. At the 6,000 au scale (Fig. 2(c)), several spiky structures can be identified. These features suggest that dense gas is streaming toward the center through multiple high-density channels. In contrast, the regions along the disk normal direction (upper right and lower left) are less dense, indicating that gas accretion does not occur there due to the presence of outflows. As shown in Figure 1(d), complex structures extend over a spatial range greater than 10,000 au. The upward-pointing spike-shaped features in this panel correspond to the cavities carved out by the outflow. Although the infalling envelope as a whole forms a flattened, sheet-like structure, it also exhibits complex features on smaller, localized scales (see also Tu et al. 2024).

Figure 3 shows the mass inflow rate onto spherical surfaces centered on the protostar at different spatial scales. In each panel, red regions indicate inflow regions with $v_r < 0$ (i.e., accretion), while black regions indicate outflow regions with $v_r > 0$. To estimate the inflow rate, we first compute the local mass flux per unit area at each point on the spherical surface as

$$\dot{m}(\theta, \phi) \equiv \rho(\theta, \phi) v_r(\theta, \phi). \quad (1)$$

Because the actual surface area associated with each sampling point varies depending on the spatial resolution of the spherical shell, we scale this local quantity to a value that would correspond to a uniform distribution over the entire sphere, and also present it in a clearer and resolution-independent form:

$$\tilde{\dot{M}}(\theta, \phi) \equiv \dot{m}(\theta, \phi) 4\pi r_0^2, \quad (2)$$

where r_0 (= 600, 3,000, 6,000, and 12,000 au) is the radius of the spherical surface. This scaled quantity should be interpreted as a diagnostic of the angular variation of the mass flux, not as the physical accretion rate. Thus, each point in Figure 3 represents the mass inflow (or outflow) rate that would be obtained if the locally measured value at that position were uniformly distributed over the entire spherical surface.

As seen in Figure 3, the inflow and outflow patterns are highly complex. However, at large scales of 12,000 au (Fig. 3(d)) and 6,000 au (Fig. 3(c)), gas predominantly escapes along the polar directions. This large-scale bipolar outflow reflects the initial magnetic field configuration, which is aligned along the north-south (vertical) direction, causing the outflow to roughly follow the initial magnetic field lines. In contrast, on smaller scales, the outflow emerges roughly along the rotation axis of the circumstellar disk and propagates in that direction (Hirano & Machida

¹ The rotationally supported disk is identified through the following procedure (Tomida et al. 2017; Hirano et al. 2020). First, we calculate the angular momentum vector of the high-density region ($n > 10^8 \text{ cm}^{-3}$) and determine its direction. Next, on the plane perpendicular to this angular momentum vector, we evaluate the rotational velocity of the gas. We define the disk density threshold n_{disk} as the density above which the rotational velocity exceeds 80% of the local Keplerian velocity. Finally, the disk is defined as the region where the density is greater than n_{disk} .

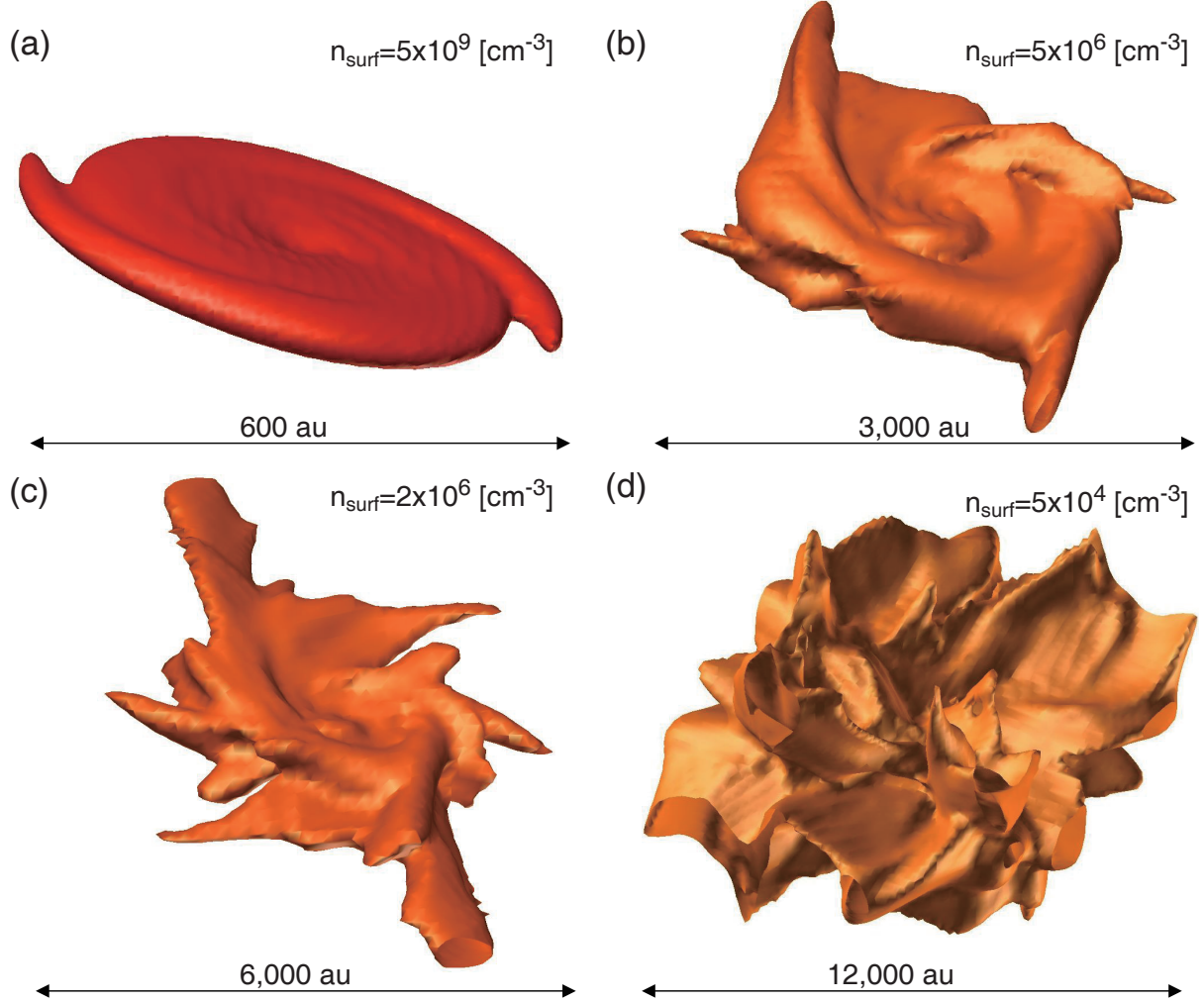


Figure 2. Three-dimensional view of the iso-density surface at number density n_{surf} , as indicated in each panel, at the same epoch as in Fig. 1. The spatial scale, also noted in each panel, differs among the panels.

2019; Machida et al. 2020). As a result, as shown in Figures 3(a) and 3(b), outflow regions appear as band-like structures distributed near the equatorial plane (see also Matsumoto et al. 2017). The inflow rate is enhanced in regions surrounding these outflows, indicating that both inflow and outflow propagate, to some extent, along the local magnetic field lines. Because the magnetic field lines are strongly twisted, the directions of inflow and outflow vary with spatial scale and can emerge from different regions on the sphere (Machida et al. 2020).

Figure 4 presents the three-dimensional patterns of infall and outflow at different spatial scales. In each panel, streamlines are plotted following the procedure:

- For each grid, the mass inflow and outflow rates are calculated on all six boundary surfaces.
- The maximum and minimum mass inflow rates, $\dot{M}_{\text{inf, max}}$ and $\dot{M}_{\text{inf, min}}$, are identified among all inflow cells.
- A threshold value $\dot{M}_{\text{inf, thr}}$ is defined as

$$\dot{M}_{\text{inf, thr}} = 10^p, \quad \text{where } p = \frac{1}{2} \left[\log_{10} (\dot{M}_{\text{inf, max}}) + \log_{10} (\dot{M}_{\text{inf, min}}) \right]. \quad (3)$$

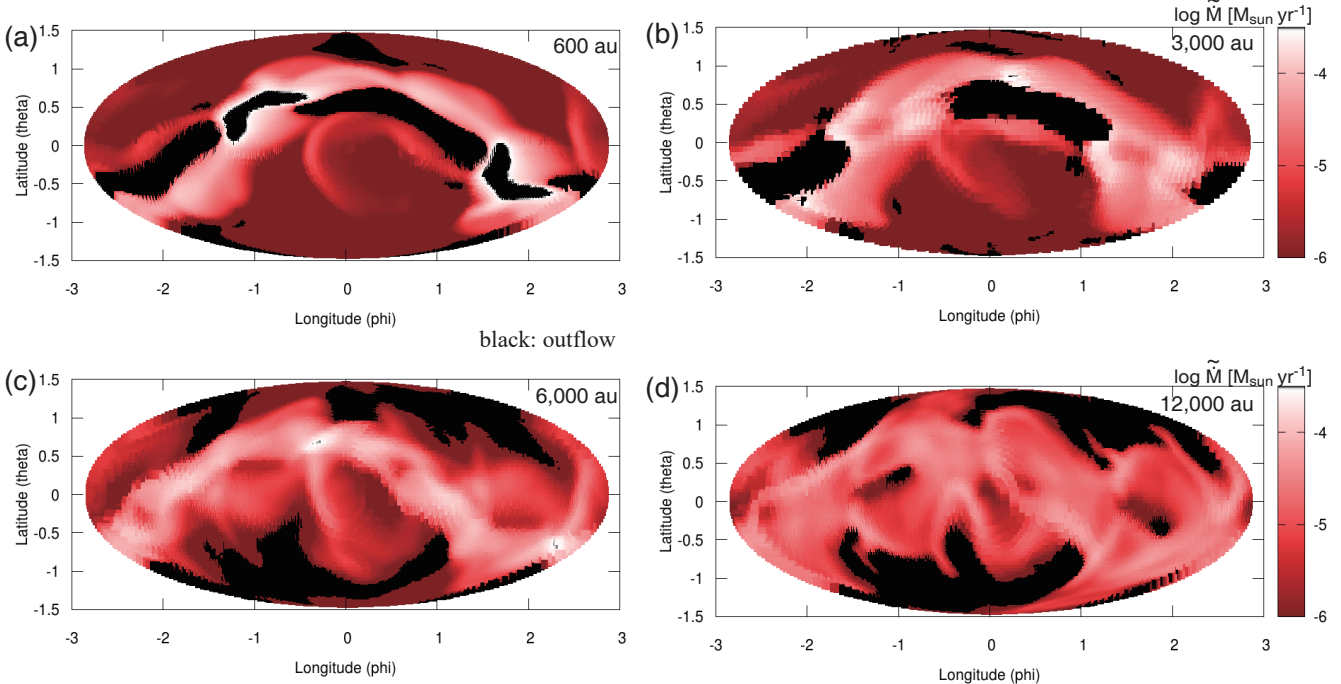


Figure 3. Mass inflow rates $\tilde{M}(\theta, \phi)$ onto spherical surfaces at radii of 600 au (panel (a)), 3,000 au (panel (b)), 6,000 au (panel (c)), and 12,000 au (panel (d)), at the same epoch as in Fig. 1. The black regions correspond to outflowing gas with $v_r > 0$. The vertical and horizontal axes represent latitude ($-\pi/2 < \theta < \pi/2$) and longitude ($-\pi < \phi < \pi$), respectively, in radians. Note that the axes correspond to spherical angles, not to the disk plane. Since the disk orientation varies with radius as the inflow moves inward, a single well-defined disk midplane cannot be drawn in this projection.

- Cells with infall rates exceeding the threshold ($\dot{M}_{\text{inf}} > \dot{M}_{\text{inf, thr}}$) are selected.
- Streamlines are integrated only from these selected cells on the six boundary surfaces.

A more detailed description of how the streamlines are plotted is provided in Appendix §A. In the second row of Figure 4, regions with radial velocities exceeding the sound speed ($v_r > c_s$) are shown as outflows (green surfaces). Almost all regions outside the outflow correspond to the infalling envelope, where gas is falling toward the center. As a result, the streamlines in Figure 4 highlight only those regions with relatively high infall rates within the overall infall. As shown in Figure 4(a), the infall pattern is highly asymmetric even at the 50,000 au scale. Prominent streams directed toward the center are clearly seen from the lower left and upper right directions. In addition, a narrow, band-like stream runs from top to bottom. A figure identical to Figure 4, but viewed from different angles, is provided in Appendix §B.

In Figure 4(b), multiple converging streams are observed, indicating that inflow or accretion occurs primarily through several distinct channels. In Figure 4(c), although a disk-like structure is present at the center, the infalling streams approach from above and below the disk plane, wrapping around its outer edges. In other words, inflow onto the disk occurs preferentially from specific regions near the disk midplane.

Magnetic field lines (red) are also plotted in panels (d)–(f) of Figure 4. The field lines are integrated from the high-density regions near the center and trace the stronger magnetic fields at each spatial scale. These visualizations therefore highlight the structure of the relatively strong magnetic field at each scale. Both configurations, where the magnetic field lines are perpendicular and parallel to the streams, are present. The details of the relationship between the gas flow direction and the magnetic field orientation will be presented in a subsequent paper.

4. DISCUSSION

In the classical picture, if strong initial turbulence is not assumed in the molecular cloud core, the mass accretion onto the disk and its surroundings is expected to remain nearly constant over short to moderate timescales, and then

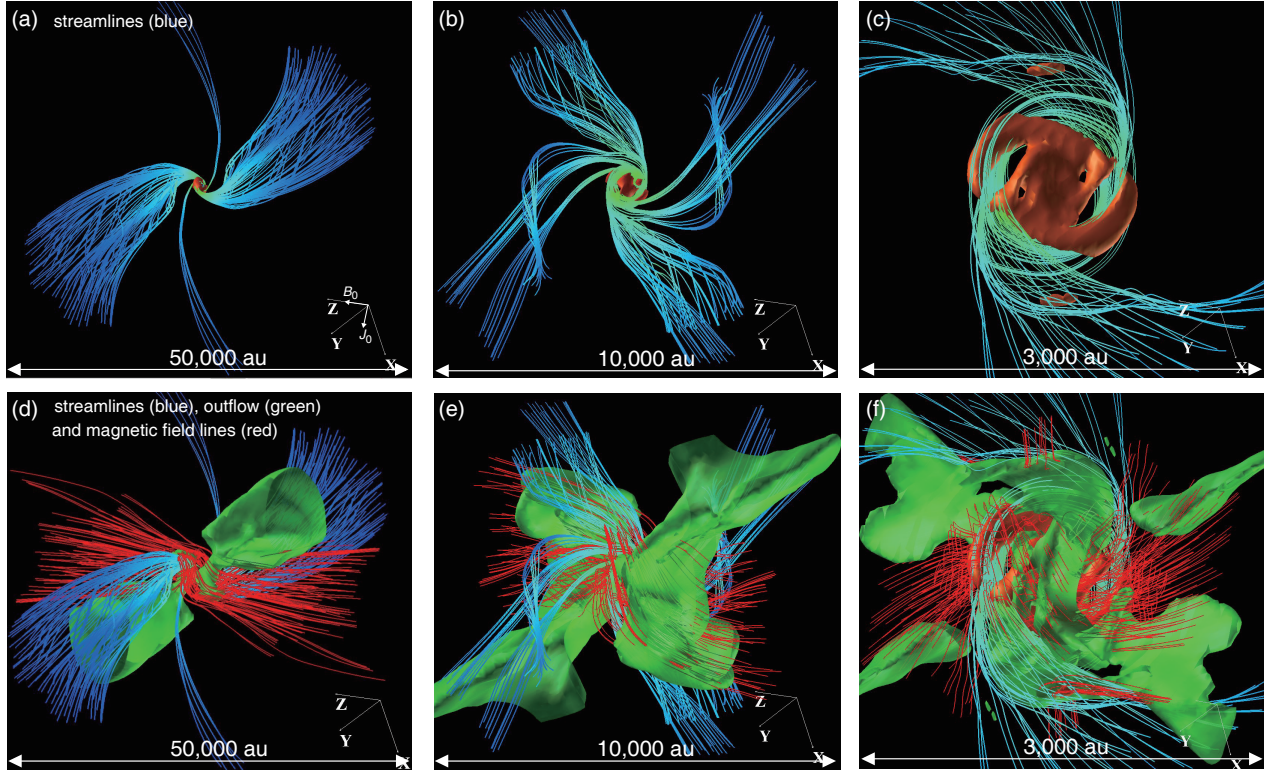


Figure 4. (a)–(c): Three-dimensional view of streamlines (blue lines) and high-density regions (brown), shown at different spatial scales, at the same epoch as in Fig. 1. (d)–(f): Outflowing gas with $v_r > c_s$ (green surfaces) and magnetic field lines (red lines) are added to the structures shown in panels (a)–(c). The spatial scale is indicated in each panel. The Cartesian x -, y -, and z -axes are shown at the bottom right corner of each panel. The initial directions of the magnetic field B_0 and angular momentum J_0 are indicated in panel (a).

gradually decline over longer timescales (Larson 2003; Vorobyov & Basu 2005). In reality, however, the pseudodisk or infalling envelope undergoes continuous morphological changes. This evolution is driven not only by magnetic and rotational effects but also by the development of protostellar outflows. Therefore, even without considering external factors such as gas inflow or clump infall from outside the core, or internal factors such as initial turbulence, gas accretion onto the central region and the disk can be intrinsically time variable.

Figure 5(a) shows the time variability of the mass infall (or accretion) rate at different spatial scales. The mass infall rate on each grid is estimated according to Equation (7) in Machida & Basu (2024). In the regions near the disk (at 370 au and 750 au), the infall rate onto the central region begins to fluctuate significantly after $t_{\text{ps}} > 40,000$ – $50,000$ yr. This variability arises from the twisted pseudodisk, which is created by magnetic field lines distorted by the rotation near the center. In addition, magnetic braking facilitates inward gas motion by removing angular momentum, while the amplification and distortion of the magnetic field suppress accretion. In regions where magnetic field lines are aligned straight toward the center, gas can accrete smoothly. In contrast, when the field lines are twisted, the flow spirals along the distorted lines, resulting in a lower inflow rate (or slower accretion) compared to the straight-line case. As shown in Figure 5(a), the inflow rate at 1,500 au begins to fluctuate after $t_{\text{ps}} > 80,000$ yr. The evolution of the pseudodisk (or infalling envelope) and the magnetic field configuration proceeds from the inside out. As a result, the time variability and spatial anisotropy of infall become more pronounced on larger scales over time.

Figure 5(b) shows the time variability of the mass outflow rate, and Figure 5(c) shows the ratio of the mass inflow rate to the mass outflow rate. Similar to the mass inflow rate, the mass outflow rate also exhibits strong time variability. When the mass inflow rate increases, a greater amount of gravitational energy is released by the infalling gas, which

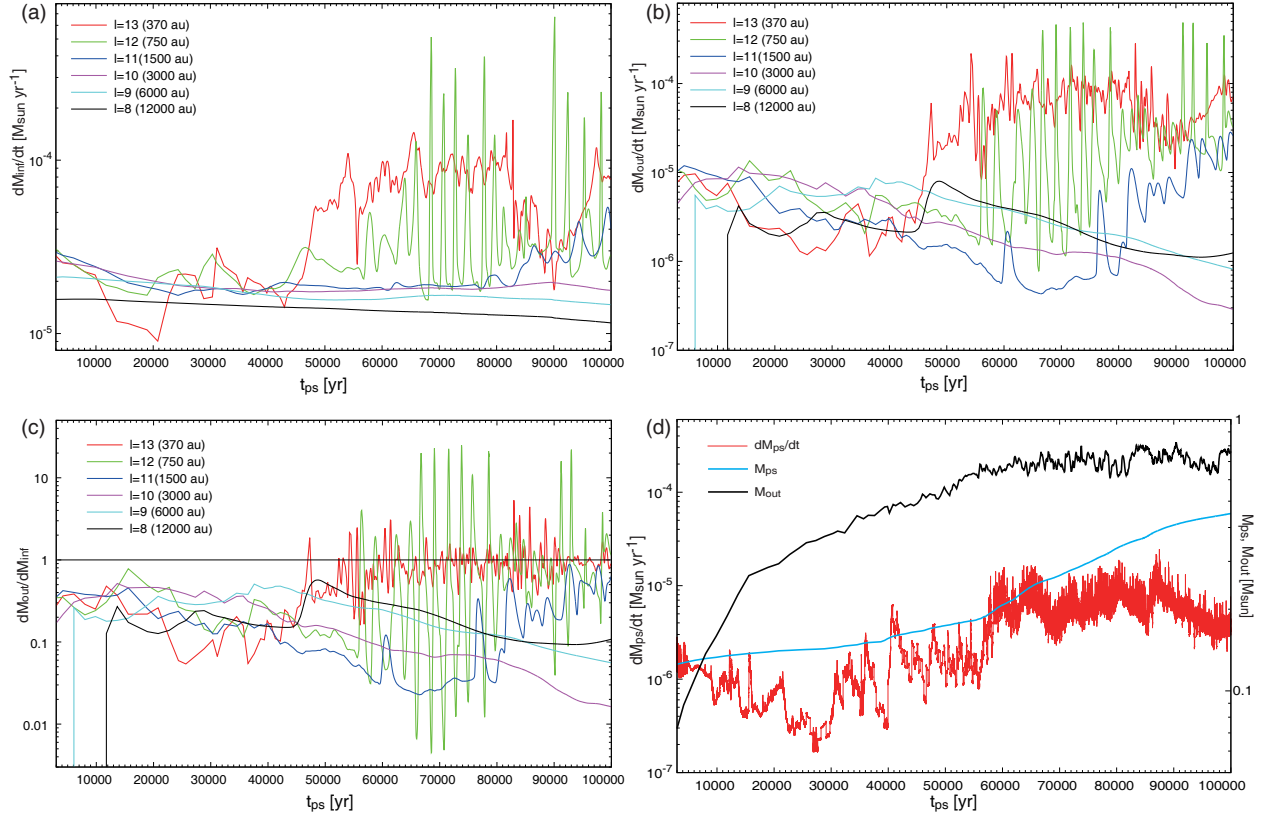


Figure 5. (a)–(c): Time evolution of the mass inflow rate \dot{M}_{infl} (panel (a)), the mass outflow rate \dot{M}_{out} (panel (b)), and the ratio of outflow to inflow rates $\dot{M}_{\text{out}}/\dot{M}_{\text{infl}}$ (panel (c)) at different spatial scales, corresponding to grid levels $l = 8$ – 13 , plotted against the elapsed time t_{ps} after protostellar formation. (d): Time evolution of the mass accretion rate onto the protostar (sink) is shown on the left axis, while the protostellar mass and outflow mass are shown on the right axis, all as functions of t_{ps} .

leads to an increase in the outflow rate (Matsushita et al. 2017, 2018). In addition, when a strong outflow appears, it can sweep up the infalling gas and eject it outward. As a result, the ratio of the mass outflow rate to the inflow rate often exceeds unity, as seen in Figure 5(c). Figure 5(c) also indicates that a nonnegligible fraction of the gas is ejected by the outflow. The extent to which outflow affects the inflow rate is still unclear, and we will explore this in a subsequent paper.

Figure 5(d) shows the mass accretion rate onto the protostar (sink) and the time evolution of the protostellar and outflow masses. The accretion rate onto the central protostar is primarily controlled by the physical condition of the disk (such as magnetic field strength and Toomre's Q), but it is also affected by the accretion from the infalling envelope onto the disk. When the accretion onto the disk varies strongly over time, the accretion rate onto the protostar also shows significant time variability, as seen in Figures 5(a) and 5(d). However, the timescale of the mass inflow (or accretion) from the infalling envelope to the disk ($\gtrsim 1,000$ yr) differs significantly from that of the accretion from the disk to the protostar ($\lesssim 100$ yr). The short-term variability in the accretion rate onto the protostar is determined by the growth and decay of nonaxisymmetric structures caused by the disk gravitational instability (Machida et al. 2010; Tomida et al. 2017; Machida & Basu 2019; Hirano et al. 2020; Machida et al. 2020) in the inner disk region. Figure 6 shows that, although the morphological change is not very large, the structure of the high-density part of the disk near the protostar changes on a relatively short timescale of ~ 100 yr. Therefore, the short-term variability ($\lesssim 100$ yr) seen in Figure 6(d) should be attributed to the time-dependent structural evolution of the high-density inner disk, which strongly affects the mass accretion from the disk onto the protostar. On the other hand, variability

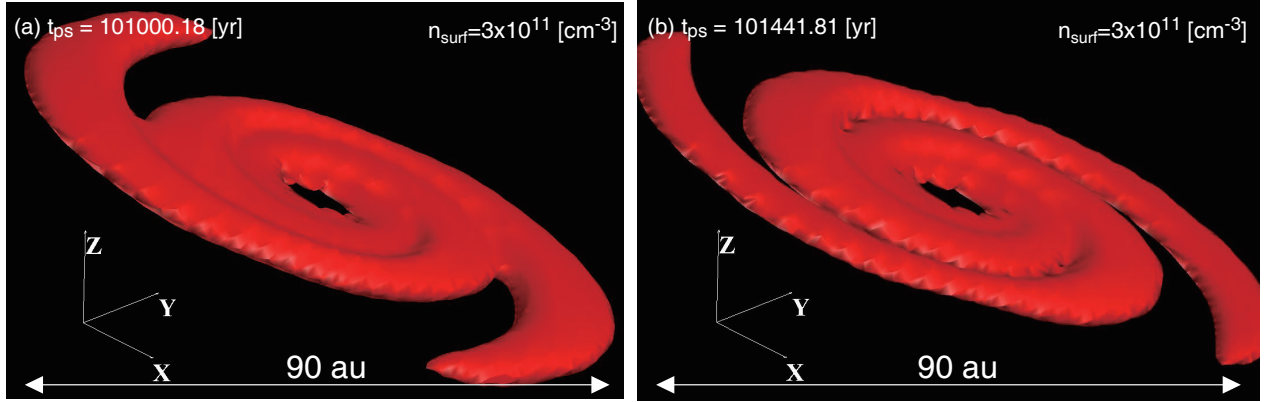


Figure 6. Three-dimensional view of the iso-density surface at a number density of $n_{\text{surf}} = 3.1 \times 10^{11} \text{ cm}^{-3}$ at $t_{\text{ps}} = 101,000.18 \text{ yr}$ (a) and $t_{\text{ps}} = 101,441.81 \text{ yr}$ (b). The high-density part of the disk is extracted to emphasize the nonaxisymmetric structure around the protostar. The spatial scale is indicated in each panel.

on timescales of $\gtrsim 1,000 \text{ yr}$ should be attributed to the mass infall from the twisted pseudodisk or complex infalling envelope. Figure 5(d) also shows that the outflow mass exceeds the protostellar mass at all times, which indicates that a substantial amount of gas is ejected even when the infalling envelope has a complex structure.

5. SUMMARY

We investigated the long-term evolution of an isolated, non-turbulent prestellar core with a 30° misalignment between the magnetic field and rotation axis. The calculation followed the evolution for over 100,000 yr after protostar formation. A pseudodisk forms during collapse due to magnetic forces, enclosing the rotationally supported disk and acting as the infalling envelope. In the misaligned model, the magnetic field is strongly twisted after disk formation, producing a highly deformed pseudodisk. This complexity spreads outward over time, and by 50,000 yr, the pseudodisk shows irregular structures on scales of $\lesssim 5,000\text{--}10,000 \text{ au}$.

The complex structure of the infalling envelope leads to substantial temporal variations in the mass inflow rate onto the disk. Infall onto the disk occurs through multiple channels rather than uniformly. We found that an asymmetric infalling envelope and asymmetric mass inflow onto the disk naturally arise from the intrinsic dynamics of the collapsing core. These asymmetric features appear even without external gas inflow, the infall of small clumps, or internal turbulence. In other words, we demonstrate that asymmetric inflow can originate from internal processes.

ACKNOWLEDGEMENTS

This research used the computational resources of the HPCI system provided by the Cyber Science Center at Tohoku University and the Cybermedia Center at Osaka University (Project ID: hp230035, hp240010, hp250007). Simulations reported in this paper were also performed by 2024, 2025 Koubo Kadai on Earth Simulator (NEC SX-ACE) at JAMSTEC. The present study was supported by JSPS KAKENHI Grant (JP25K07369: MNM, JP21H01123 and JP21K13960: SH). This work was supported by a NAOJ ALMA Scientific Research grant (No. 2022-22B). S.B. was supported by a Discovery Grant from NSERC.

REFERENCES

Basu, S., & Mouschovias, T. C. 1994, *ApJ*, 432, 720, doi: [10.1086/174611](https://doi.org/10.1086/174611)
 —. 1995a, *ApJ*, 452, 386, doi: [10.1086/176310](https://doi.org/10.1086/176310)
 —. 1995b, *ApJ*, 453, 271, doi: [10.1086/176387](https://doi.org/10.1086/176387)

Basu, S., Sharkawi, M., & Machida, M. N. 2024, *ApJ*, 964, 116, doi: [10.3847/1538-4357/ad1bf3](https://doi.org/10.3847/1538-4357/ad1bf3)
 Caselli, P., Benson, P. J., Myers, P. C., & Tafalla, M. 2002, *ApJ*, 572, 238, doi: [10.1086/340195](https://doi.org/10.1086/340195)

Choudhury, S., Kim, J., Caselli, P., Lee, C. W., & Pineda, J. E. 2025, *A&A*, 696, A190, doi: [10.1051/0004-6361/202453281](https://doi.org/10.1051/0004-6361/202453281)

Crutcher, R. M., Wandelt, B., Heiles, C., Falgarone, E., & Troland, T. H. 2010, *ApJ*, 725, 466, doi: [10.1088/0004-637X/725/1/466](https://doi.org/10.1088/0004-637X/725/1/466)

Fielder, S. D., Kirk, H., Dunham, M. M., & Offner, S. S. R. 2024, *ApJ*, 968, 10, doi: [10.3847/1538-4357/ad3d56](https://doi.org/10.3847/1538-4357/ad3d56)

Galli, D., & Shu, F. H. 1993, *ApJ*, 417, 243, doi: [10.1086/173306](https://doi.org/10.1086/173306)

Garufi, A., Podio, L., Codella, C., et al. 2022, *A&A*, 658, A104, doi: [10.1051/0004-6361/202141264](https://doi.org/10.1051/0004-6361/202141264)

Hirano, S., Aikawa, Y., & Machida, M. N. 2025, *ApJ*, 982, 166, doi: [10.3847/1538-4357/adb96f](https://doi.org/10.3847/1538-4357/adb96f)

Hirano, S., & Machida, M. N. 2019, *MNRAS*, 485, 4667, doi: [10.1093/mnras/stz740](https://doi.org/10.1093/mnras/stz740)

Hirano, S., Tsukamoto, Y., Basu, S., & Machida, M. N. 2020, *ApJ*, 898, 118, doi: [10.3847/1538-4357/ab9f9d](https://doi.org/10.3847/1538-4357/ab9f9d)

Hull, C. L. H., Plambeck, R. L., Bolatto, A. D., et al. 2013, *ApJ*, 768, 159, doi: [10.1088/0004-637X/768/2/159](https://doi.org/10.1088/0004-637X/768/2/159)

Kataoka, A., Machida, M. N., & Tomisaka, K. 2012, *ApJ*, 761, 40, doi: [10.1088/0004-637X/761/1/40](https://doi.org/10.1088/0004-637X/761/1/40)

Kido, M., Yen, H.-W., Sai, J., et al. 2025, *ApJ*, 985, 166, doi: [10.3847/1538-4357/adc72a](https://doi.org/10.3847/1538-4357/adc72a)

Larson, R. B. 2003, *Reports on Progress in Physics*, 66, 1651, doi: [10.1088/0034-4885/66/10/R03](https://doi.org/10.1088/0034-4885/66/10/R03)

Machida, M. N. 2021, *MNRAS*, 508, 3208, doi: [10.1093/mnras/stab2626](https://doi.org/10.1093/mnras/stab2626)

Machida, M. N., & Basu, S. 2019, *ApJ*, 876, 149, doi: [10.3847/1538-4357/ab18a7](https://doi.org/10.3847/1538-4357/ab18a7)

—. 2024, *ApJ*, 970, 41, doi: [10.3847/1538-4357/ad4997](https://doi.org/10.3847/1538-4357/ad4997)

Machida, M. N., Hirano, S., & Kitta, H. 2020, *MNRAS*, 491, 2180, doi: [10.1093/mnras/stz3159](https://doi.org/10.1093/mnras/stz3159)

Machida, M. N., & Hosokawa, T. 2013, *MNRAS*, 431, 1719, doi: [10.1093/mnras/stt291](https://doi.org/10.1093/mnras/stt291)

—. 2020, *MNRAS*, 499, 4490, doi: [10.1093/mnras/staa3139](https://doi.org/10.1093/mnras/staa3139)

Machida, M. N., Inutsuka, S.-i., & Matsumoto, T. 2006, *ApJL*, 647, L151, doi: [10.1086/507179](https://doi.org/10.1086/507179)

—. 2010, *ApJ*, 724, 1006, doi: [10.1088/0004-637X/724/2/1006](https://doi.org/10.1088/0004-637X/724/2/1006)

—. 2014, *MNRAS*, 438, 2278, doi: [10.1093/mnras/stt2343](https://doi.org/10.1093/mnras/stt2343)

Machida, M. N., Matsumoto, T., & Inutsuka, S.-i. 2016, *MNRAS*, 463, 4246, doi: [10.1093/mnras/stw2256](https://doi.org/10.1093/mnras/stw2256)

Machida, M. N., Matsumoto, T., Tomisaka, K., & Hanawa, T. 2005, *MNRAS*, 362, 369, doi: [10.1111/j.1365-2966.2005.09297.x](https://doi.org/10.1111/j.1365-2966.2005.09297.x)

Machida, M. N., Tomisaka, K., & Matsumoto, T. 2004, *MNRAS*, 348, L1, doi: [10.1111/j.1365-2966.2004.07402.x](https://doi.org/10.1111/j.1365-2966.2004.07402.x)

Matsumoto, T., Machida, M. N., & Inutsuka, S.-i. 2017, *ApJ*, 839, 69, doi: [10.3847/1538-4357/aa6a1c](https://doi.org/10.3847/1538-4357/aa6a1c)

Matsushita, Y., Machida, M. N., Sakurai, Y., & Hosokawa, T. 2017, *MNRAS*, 470, 1026, doi: [10.1093/mnras/stx893](https://doi.org/10.1093/mnras/stx893)

Matsushita, Y., Sakurai, Y., Hosokawa, T., & Machida, M. N. 2018, *MNRAS*, 475, 391, doi: [10.1093/mnras/stx3070](https://doi.org/10.1093/mnras/stx3070)

Misugi, Y., Inutsuka, S.-i., Arzoumanian, D., & Tsukamoto, Y. 2024, *ApJ*, 963, 106, doi: [10.3847/1538-4357/ad1990](https://doi.org/10.3847/1538-4357/ad1990)

Pineda, J. E., Segura-Cox, D., Caselli, P., et al. 2020, *Nature Astronomy*, 4, 1158, doi: [10.1038/s41550-020-1150-z](https://doi.org/10.1038/s41550-020-1150-z)

Pineda, J. E., Arzoumanian, D., Andre, P., et al. 2023, in *Astronomical Society of the Pacific Conference Series*, Vol. 534, *Protostars and Planets VII*, ed. S. Inutsuka, Y. Aikawa, T. Muto, K. Tomida, & M. Tamura, 233, doi: [10.48550/arXiv.2205.03935](https://doi.org/10.48550/arXiv.2205.03935)

Planck Collaboration, Ade, P. A. R., Aghanim, N., et al. 2016, *A&A*, 586, A138, doi: [10.1051/0004-6361/201525896](https://doi.org/10.1051/0004-6361/201525896)

Shinnaga, H., Novak, G., Vaillancourt, J. E., et al. 2012, *ApJL*, 750, L29, doi: [10.1088/2041-8205/750/2/L29](https://doi.org/10.1088/2041-8205/750/2/L29)

Tanious, M., Le Gal, R., Neri, R., et al. 2024, *A&A*, 687, A92, doi: [10.1051/0004-6361/202348785](https://doi.org/10.1051/0004-6361/202348785)

Tokuda, K., Fukaya, N., Tachihara, K., et al. 2023, *ApJL*, 956, L16, doi: [10.3847/2041-8213/acfca9](https://doi.org/10.3847/2041-8213/acfca9)

Tokuda, K., Onishi, T., Saigo, K., et al. 2014, *ApJL*, 789, L4, doi: [10.1088/2041-8205/789/1/L4](https://doi.org/10.1088/2041-8205/789/1/L4)

Tokuda, K., Onishi, T., Matsumoto, T., et al. 2016, *ApJ*, 826, 26, doi: [10.3847/0004-637X/826/1/26](https://doi.org/10.3847/0004-637X/826/1/26)

Tokuda, K., Harada, N., Omura, M., et al. 2024, *ApJ*, 965, 99, doi: [10.3847/1538-4357/ad2f9a](https://doi.org/10.3847/1538-4357/ad2f9a)

Tomida, K., Machida, M. N., Hosokawa, T., Sakurai, Y., & Lin, C. H. 2017, *ApJL*, 835, L11, doi: [10.3847/2041-8213/835/1/L11](https://doi.org/10.3847/2041-8213/835/1/L11)

Tomisaka, K. 1995, *ApJ*, 438, 226, doi: [10.1086/175067](https://doi.org/10.1086/175067)

—. 1996, *PASJ*, 48, 701, doi: [10.1093/pasj/48.5.701](https://doi.org/10.1093/pasj/48.5.701)

Tsukamoto, Y., Maury, A., Commercon, B., et al. 2023, in *Astronomical Society of the Pacific Conference Series*, Vol. 534, *Protostars and Planets VII*, ed. S. Inutsuka, Y. Aikawa, T. Muto, K. Tomida, & M. Tamura, 317, doi: [10.48550/arXiv.2209.13765](https://doi.org/10.48550/arXiv.2209.13765)

Tu, Y., Li, Z.-Y., Lam, K. H., Tomida, K., & Hsu, C.-Y. 2024, *MNRAS*, 527, 10131, doi: [10.1093/mnras/stad3843](https://doi.org/10.1093/mnras/stad3843)

Valdivia-Mena, M. T., Pineda, J. E., Segura-Cox, D. M., et al. 2022, *A&A*, 667, A12, doi: [10.1051/0004-6361/202243310](https://doi.org/10.1051/0004-6361/202243310)

Vorobyov, E. I., & Basu, S. 2005, *MNRAS*, 360, 675, doi: [10.1111/j.1365-2966.2005.09062.x](https://doi.org/10.1111/j.1365-2966.2005.09062.x)

Yen, H.-W., Gu, P.-G., Hirano, N., et al. 2019, *ApJ*, 880, 69, doi: [10.3847/1538-4357/ab29f8](https://doi.org/10.3847/1538-4357/ab29f8)

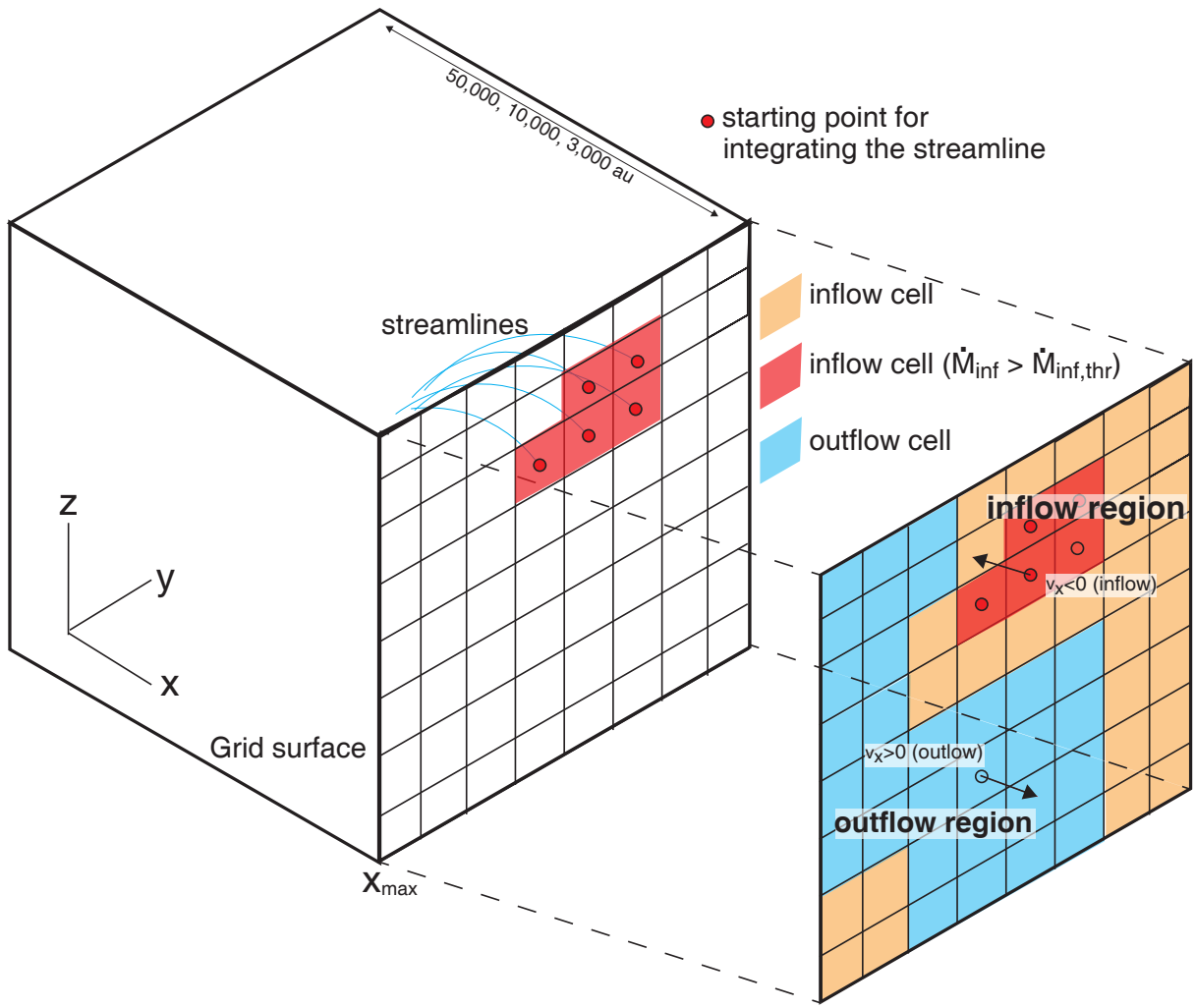


Figure 7. Schematic illustration of how the streamlines are plotted. For clarity, the procedure is shown only on the grid surface of $x > 0$ (or $x = x_{\text{max}}$).

APPENDIX

A. PROCEDURE TO PLOTTING STREAMLINES

Figure 7 illustrates the procedure used to plot the streamlines in Figures 4 and 8. For clarity, the explanation is shown only for the surface at $x > 0$ (or $x = x_{\text{max}}$), but the same procedure is applied to all six outer surfaces of the Cartesian grid with box sizes of 50,000, 10,000, and 3,000 au.

As described in Section 3, inflow and outflow regions are identified on each surface using the velocity component normal to that surface (e.g., v_x on the $x > 0$ plane). Among the inflow cells, we select those whose mass inflow rate exceeds the threshold value $\dot{M}_{\text{inf,thr}}$. Streamlines are then integrated inward from these selected surface cells using the full three-dimensional velocity vector at each grid cell. This procedure allows us to trace the dominant flow paths from

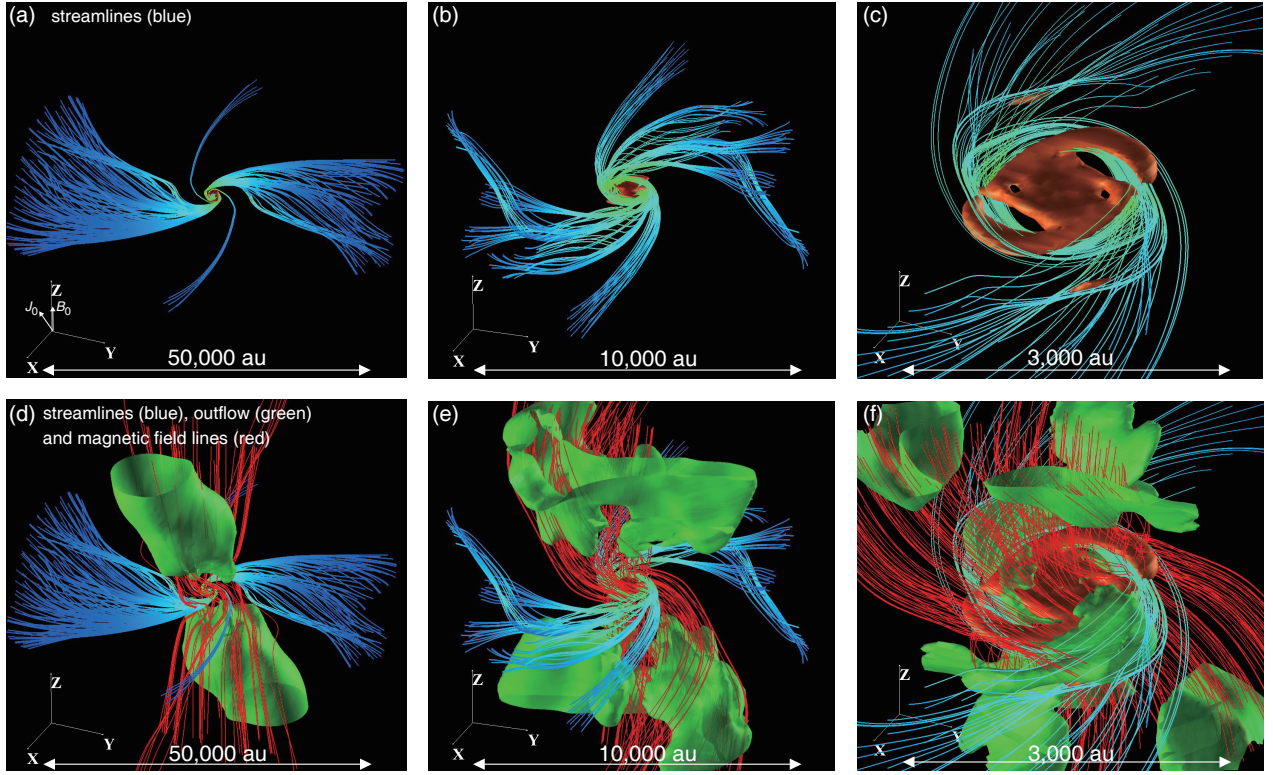


Figure 8. Same as Fig. 4, but shown from a different viewing angle. The initial directions of the magnetic field B_0 and angular momentum J_0 are indicated in panel (a).

the outer boundary toward the central region while avoiding the ambiguity associated with tangential fluxes between neighboring surface cells.

B. THREE-DIMENSIONAL VIEW OF STREAMLINES, MAGNETIC FIELD LINES AND OUTFLOWS

Figure 8 is the same as Fig. 4, but viewed from different angles. For reference, the initial directions of the magnetic field B_0 and angular momentum J_0 are indicated in panel (a). Panels (d)–(f) show that the outflow (green surfaces) propagates roughly along the z -direction. The magnetic field lines (red) are also roughly aligned with the z -axis on large scales (panel d), while exhibiting a highly twisted and complex morphology on smaller scales (panel f). The streamlines (blue) indicate that the infalling gas approaches the central region mainly from lateral directions, approximately perpendicular to the initial B_0 (or equivalently, the z) direction.